

Model Studies on Solid Electrolyte Interphase Formation on Graphite Electrodes in Ethylene Carbonate and Dimethyl Carbonate II: Graphite Powder Electrodes

Isabella Weber,^[a, b, c] Bin Wang,^[b] Carina Bodirsky,^[b] Monalisa Chakraborty,^[b] Mario Wachtler,^[d] Thomas Diemant,^[b] Johannes Schnaidt,^[a, c] and R. Jürgen Behm^{*[a, b]}

As part of a systematic study on the formation and composition of the solid electrolyte interphase (SEI) in lithium-ion batteries (LIBs), going stepwise from highly idealized electrodes such as highly oriented pyrolytic graphite and conditions such as ultrahigh vacuum conditions to more realistic materials and reaction conditions, we investigated the decomposition of simplified electrolytes (ethylene carbonate (EC) + 1 M LiPF₆ and dimethyl carbonate (DMC) + 1 M LiPF₆) at binder-free graphite powder model electrodes. The results obtained from cyclic

voltammetry and ex situ X-ray photoelectron spectroscopy half-cell measurements – in particular on the effect of cycling rate, solvent and electrode – are explained in terms of a mechanistic model where electrolyte decomposition occurs at the SEI | electrode interface and where transport of solvent and salt species through the growing SEI plays an important role for explaining the observed change from preferential salt decomposition to solvent decomposition with increasing cycling rate.

1. Introduction

Lithium-ion batteries (LIBs) are by now well established in portable communication devices^[1,2] and also increasingly important as power sources for automotive applications.^[3,4] Typically, they consist of electrode materials capable of inserting and de-inserting Li cations^[5–8] and blends of Li salt-containing carbonate solvents^[9–11] and additives^[12] as electrolyte. During the first charge/discharge cycles, the thermodynamically unstable electrolyte decomposes at the anode, forming a passivating interphase. This is commonly denoted as solid electrolyte interphase (SEI),^[13] which allows for continuous Li⁺ diffusion and (de-)insertion while, at the same time, passivating the electrode surface against further electrolyte decomposition and thus protecting the battery from electrolyte


depletion and electrode corrosion. The SEI is composed of a mixture of salt and solvent decomposition products depending on the solvent,^[14,15] salt^[16,17] and possible additives,^[12,18,19] but also on the nature of the electrode material.^[20–26] It is known to decisively affect the battery performance,^[27–31] which is why its formation and composition have been investigated for decades. Nevertheless, a detailed understanding of the SEI formation mechanisms is still missing, mainly due to the complex situation in realistic LIBs which include electrode materials, electrolyte and reaction conditions. We thus started an extensive study of the SEI formation process, employing materials with reduced complexity such as structurally well-defined highly-oriented pyrolytic graphite (HOPG) as model systems^[32,33] and simplified reaction conditions such as ultrahigh vacuum conditions^[32] or electrochemical measurements in single-solvent model electrolytes.^[33] In the present work, we extended this to a more realistic situation, studying the SEI formation at two different binder-free graphite powder film electrodes in 1 M LiPF₆-containing single-solvent electrolytes, either ethylene carbonate (EC) or dimethyl carbonate (DMC), which are components of the commonly used battery electrolyte LP30 (1 M LiPF₆ + EC/DMC, 1:1 v/v). Two types of graphite were studied: the first one, MAGE, is an artificial graphite produced by Hitachi Chemical Co., Ltd. which is used as anode material in high-energy LIBs. The second anode material investigated in this work, SNG, is prepared from natural graphite flakes using a lab-type mechanical spheroidization process.^[34,35] For comparison, we also characterized the SEI formation on the binder-free and binder-containing graphite powder film electrodes in LP30 electrolyte. SEI formation was first characterized by cyclic voltammetry measurements, following the current evolution upon repeated potential cycling. Analysis of the chemical surface composition was conducted by X-ray photoelectron spectroscopy (XPS). In addition, depth profiling gained informa-


[a] I. Weber, Dr. J. Schnaidt, Prof. R. J. Behm
Helmholtz-Institute Ulm (HIU) Electrochemical Energy Storage
Helmholtzstraße 11, 89081 Ulm, Germany
E-mail: juergen.behm@uni-ulm.de

[b] I. Weber, B. Wang, C. Bodirsky, M. Chakraborty, Dr. T. Diemant,
Prof. R. J. Behm
Institute of Surface Chemistry and Catalysis
Ulm University
Albert-Einstein-Allee 47, 89081 Ulm, Germany

[c] I. Weber, Dr. J. Schnaidt
Karlsruhe Institute of Technology (KIT)
P.O. Box 3640, 76021 Karlsruhe, Germany

[d] Dr. M. Wachtler
Zentrum für Sonnenenergie- und Wasserstoff-Forschung Baden-Württemberg (ZSW)
Helmholtzstraße 8, 89081 Ulm, Germany

 Supporting information for this article is available on the WWW under <https://doi.org/10.1002/celec.202001328>

 © 2020 The Authors. ChemElectroChem published by Wiley-VCH GmbH. This is an open access article under the terms of the Creative Commons Attribution Non-Commercial License, which permits use, distribution and reproduction in any medium, provided the original work is properly cited and is not used for commercial purposes.

tion also on the variation of the elemental SEI composition with increasing depth. Finally, we will compare the present results with our previous findings obtained on HOPG model electrodes in single-solvent electrolytes.^[33]

Before presenting and discussing the results, we will briefly summarize previous studies and conclusions relevant for the understanding of our data. Numerous electrochemical studies employed HOPG as a model electrode with a low defect site density to investigate the formation and composition of the SEI under structurally well-defined conditions.^[14,19,22,36–43] The results indicated a very low Li^+ intercalation capacity and the slow and inhomogeneous formation of a passivation film at the basal plane, which was proposed to be dominated by solvent decomposition.^[22,40,41] The edge plane, on the other hand, was shown to be active both for preferential salt decomposition^[22,40,41] and for Li^+ (de-)intercalation.^[43,44] Several studies reported exfoliation of the HOPG electrode, most likely induced by solvent co-intercalation (especially in DMC^[15,33]). Individual, HOPG-supported graphite particles, which were studied by electrochemical atomic force microscopy, displayed an enhanced SEI formation activity and a better cell performance, which was attributed to the higher concentration of defect sites.^[45] This is in line with our observations of the significant influence of the HOPG surface roughness on the SEI formation process.^[33] Finally, the influence of the individual electrolyte components was investigated in further model studies using single-solvent electrolytes^[15,33,39,46] instead of the typical carbonate solvent blends.

Moving on to more realistic, but still simplified, electrodes, Lucht and coworkers prepared binder-free graphite electrodes (SFG-6, TIMCAL) by electrophoretic deposition to investigate the composition of the SEI formed in LiPF_6 -containing electrolyte^[47] and in several other Li-salt-containing electrolyte blends.^[48] Nie *et al.* studied the solvent – salt interactions in LiPF_6 -based single-solvent electrolytes and observed a distinct influence of the salt concentration on the electrochemical performance of the binder-free graphite electrodes.^[49] Employing different spectroscopic techniques, they identified the semicarboxylate Li ethylene dicarbonate and Li alkoxides as the main products of ethylene carbonate reduction and LiF as the dominant reduction product of LiPF_6 decomposition.^[23] Novák *et al.* investigated the influence of surface defects on the SEI formation by modifying the structural order of the graphite (TIMREX SLX50, TIMCAL) surface via (reactive) annealing in different gases (Ar, He, H_2).^[50,51] Using binder-containing graphite electrodes without additional conductive carbon, they showed that the electrolyte decomposition and thus the formation of a passivating SEI is shifted to higher potential by a high concentration of surface defects and increasingly hinders exfoliation of the graphite.^[50,51]

Overall, this work strives at a more detailed understanding of the various structural and chemical effects on the SEI formation process and the composition of the resulting passivation layer in Li-ion batteries.

2. Results and Discussion

Both graphite materials, the artificial graphite MAGE and the processed natural graphite SNG, consist of irregular particles (with rounded edges for SNG, a result of the spheroidization process) and a highly graphitized inner structure. MAGE has an average d_{50} particle size of 24.4 μm , a specific surface area of 3.5 m^2g^{-1} and a reversible capacity of 365 mAhg^{-1} .^[52] For SNG, the corresponding values are a d_{50} particle size of 12.8 μm , a specific surface area (via N_2 sorption) of 8.6 m^2g^{-1} and a reversible capacity of 366 mAhg^{-1} .^[34] Representative transmission electron microscopy (TEM) images are presented in Figure S1 in the Supporting Information. Aside from the discrepancy in the average particle size, there are no significant differences in morphology of the graphite materials.

Thin films of these graphite powders were deposited on a glassy carbon (GC) electrode (see Experimental).

2.1. Electrochemical Electrolyte Decomposition and SEI Formation

2.1.1. Influence of the Active Material and Solvent

Cyclic voltammograms (CVs) of the two graphite materials recorded in single-solvent EC- and DMC-based electrolytes at 0.1 mVs^{-1} are displayed in Figure 1. While the nature of the electrode material has only little effect on the current densities, these are tenfold lower in DMC- than in EC-based electrolyte. A reduction peak (c_e) appears at 0.7 V in the cathodic scan of the first cycle both for the MAGE and the SNG electrode in EC-based electrolyte. In accordance with previous findings,^[15] and also with results of our own model studies on HOPG,^[33] we assign this peak to reductive electrolyte decomposition and subsequent formation of a solid electrolyte interphase (SEI). Note that, at this point, we cannot distinguish between predominant solvent decomposition and predominant salt decomposition, which will be discussed in more detail later. In DMC-based electrolyte, the first peak in the negative-going scan (c_e) of the CVs is observed at 0.8 V on MAGE and at 1.4/1.0 V on SNG, while a second set of signals (c_e) appears at 0.3 and 0.4 V, respectively. The higher-potential peaks observed in the DMC-based CVs at 0.8 V (1.4/1.0 V) on MAGE (SNG) film electrodes are most likely due to reductive processes involving residual H_2O (EC: ≤ 50 ppm, DMC: ≤ 20 ppm, glove box: < 1.0 ppm) or O_2 traces, but have also been attributed to LiPF_6 reduction previously.^[14,37] We think that the presence of $\text{H}_2\text{O}/\text{O}_2$ trace contaminations is more likely than LiPF_6 reduction. It also explains the comparatively high cathodic current densities recorded between the upper potential limit and 0.5 V in DMC-based electrolyte. Next, electrolyte decomposition (c_e) takes place at 0.3/0.4 V, in agreement with previous reports.^[15,33] Note that the onset potentials for electrolyte reduction follow a similar trend as observed in our previous experiments on HOPG electrodes cycled under the same conditions, with higher onset potentials for EC-based electrolyte.^[33] After electrolyte decomposition, stepwise Li^+ intercalation sets in at around 0.2 eV, in

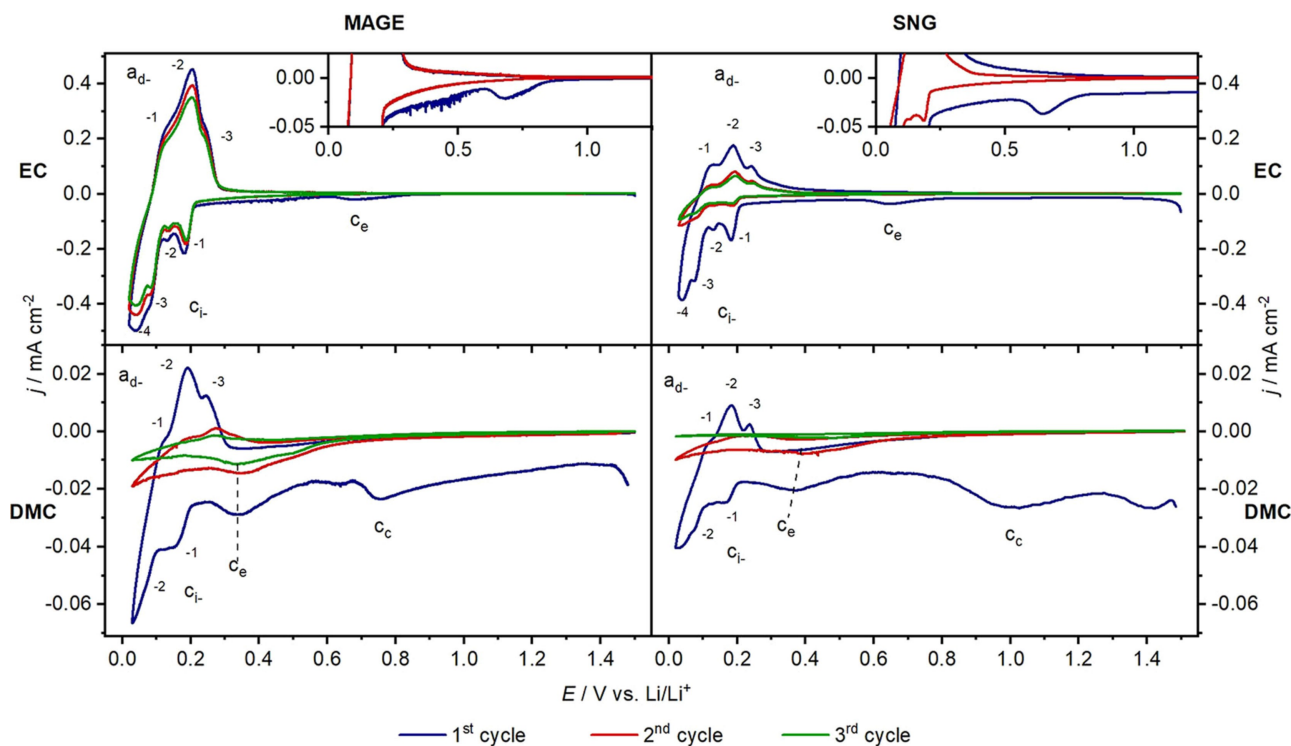


Figure 1. Cyclic voltammograms recorded on binder-free MAGE (left) and SNG (right) powder film electrodes in EC (top) and DMC (bottom) + 1 M LiPF₆ at a scan rate of 0.1 mVs⁻¹. The insets display the current at tenfold magnified scale.

accordance with previous findings.^[5] Three sharp peaks (c_{11} , c_{12} , c_{14}) appear at 0.2, 0.1 and 0.05 V for both MAGE and SNG cycled in EC-based electrolyte, where the peak at 0.05 V (c_{14}) is preceded by a small shoulder at 0.08 V (c_{13}). Cycling in DMC-based electrolyte, however, we only observed two intercalation steps with lower and broader signals at 0.2 and 0.07 V (c_{11} and c_{12} , respectively) for both graphite electrodes. The lower resolution of the Li⁺ intercalation peaks and the overall lower current densities observed for DMC-based electrolyte (as compared to the EC-based one) most likely indicate that the graphite material has been at least partially exfoliated as a result of solvent co-intercalation occurring between 0.6 and 0.2 mV.

In the anodic scan of the first cycle, Li⁺ de-intercalation peaks (a_{d1} – a_{d3}) are observed at potentials of 0.1, 0.2 and 0.25 V, both for EC-based and for DMC-based electrolyte. Interestingly, the current traces in the (de-)intercalation potential range are similar for the two electrode materials, but differ for the two solvents. Hence, the influence of the graphite material is less pronounced compared to the influence of the solvent. For both the MAGE and the SNG electrodes, there are no distinct peaks at higher potentials. When cycling in EC-based electrolyte, small anodic currents remain directly after Li⁺ de-intercalation, while for DMC-based electrolyte, cathodic currents are observed in this potential range, indicating continuous reduction processes at the graphite|electrolyte interface. These are probably a result of exfoliation of the graphite, creating new surfaces which are overgrown by an SEI film. Net cathodic currents during Li⁺ de-intercalation were reported also by Nie *et al.* on

binder-free graphite electrodes in propylene carbonate (PC) + 2.4 M LiPF₆ (0.05 mVs⁻¹).^[23] Interestingly, we obtained a similar behavior of the CVs recorded both for the MAGE and SNG electrodes in DMC-based electrolyte as reported by Nie *et al.* at faster scan rates (see Figure S2 and discussion in the following section). In the study of Nie *et al.*, the overall currents observed during and after Li⁺ de-intercalation were found to be cathodic at lower salt concentration, while at higher concentration, net anodic currents were reported.^[23] In our measurements, we found net anodic currents in DMC-based electrolyte for much lower salt concentrations, indicating that SEI formation in DMC-based electrolyte is more efficient in inhibiting electrolyte decomposition than SEI-formation in PC-based electrolyte, despite the occurring graphite exfoliation in the former electrolyte.

In the second cathodic scan in EC-based electrolyte we did not observe the electrolyte decomposition peak c_e at 0.7 V anymore, neither for the MAGE nor for the SNG electrode. Hence, the electrodes are completely passivated for this process, as expected for successful SEI formation. In DMC-based electrolyte, in contrast, we still observe reductive electrolyte decomposition at 0.3–0.4 V in the second (and third) cycle for both graphite electrodes, retaining about half (one third) of the current density observed in the first cycle. These ongoing reductive processes are most likely also responsible for the negative currents observed in the anodic scan.

While the loss of Li⁺ (de-)intercalation currents is negligible in the first three cycles for MAGE|EC, this is different for SNG|EC, where half of the Li⁺ (de-)intercalation current is lost

in the second cycle. In the third cycle, the loss is less pronounced. In DMC-based electrolyte, the current density for Li^+ (de-)intercalation drops by two third from the first to the second cycle and again by about half in the third cycle. We suggest that the decreasing Li^+ (de-)insertion capacity is at least in part due to exfoliation, which disrupts the graphite lattice and reduces the number of Li^+ storage sites. In addition, this is caused by both SEI formation and irreversible Li^+ intercalation, where the latter increasingly blocks sites for reversible Li^+ intercalation (irreversible specific charge^[5]). Alternatively, it could also be due to increasing kinetic limitations for thicker SEI layers, assuming that the SEI grows at the interface between SEI and electrode rather than between SEI and electrolyte (see below), or due to a loss of active material from the model electrodes due to the lack of binder. This will be discussed in more detail at the end of the paper. Finally, for both electrodes, the individual peaks denoting stepwise intercalation disappear after the first cycle in DMC-based electrolyte and only a broad (de-)intercalation signal remains instead. Most simply, this can be explained by continued graphite exfoliation and by the formation of an inhomogeneous SEI with local differences in the Li^+ transport properties.

2.1.2. Influence of the Scan Rate

Figure 2 shows the influence of different scan rates (10, 1, and 0.1 mVs^{-1}), simulating different charge/discharge rates, on the characteristics of the first cycle recorded on MAGE and SNG in EC- and DMC-based electrolyte (for more cycles, see Figure S2). The CVs recorded at 0.1 mVs^{-1} were described above. The CVs

cycled at 1 and 10 mVs^{-1} display essentially the same characteristics, albeit with shifted peak potentials and broadened peaks due to the increase in scan speed, both for electrolyte decomposition (c_e) and Li^+ (de-)intercalation. At the same time, the overall current densities increase with increasing cycling speed. This is especially pronounced for the graphite materials in DMC-based electrolyte cycled at 10 mVs^{-1} , where the current density in the Li^+ (de-)intercalation region is of the same order of magnitude as that recorded for the graphite materials during cycling in EC-based electrolyte (C|EC). Note that, as described above, the current density for the graphite powder electrodes in DMC-based electrolyte (C|DMC) is only about one tenth compared to that for C|EC when cycling at 0.1 mVs^{-1} . We suggest that this discrepancy is due to a rather slow passivating process in DMC-based electrolyte, where only at slow scan rates this has enough time for efficient passivation despite the graphite exfoliation, leading to lower current densities. For cycling at 10 mVs^{-1} , in contrast, the time is too short and the scan reaches the Li^+ intercalation region before the surface is significantly passivated against this process. It is also worth mentioning that, for cycling at 1 and 10 mVs^{-1} , the peak potentials for electrolyte decomposition (0.6 V) are very similar in both EC- and DMC-based electrolyte, whereas at 0.1 mVs^{-1} , the respective peaks appear at rather different potentials (0.7 V (EC) and 0.3–0.4 V (DMC), respectively). This is true for both MAGE and SNG electrodes. Obviously, with increasing scan rate, the peak at 0.3–0.4 V disappears, while a new one at 0.6 V grows in (Figure 2). This would be compatible with two different processes, where the low-potential process is slow, and hence only observed at lower scan rates, while the upper one is fast(er), but can proceed only on the surface area not yet modified by SEI formation. As will be discussed later when

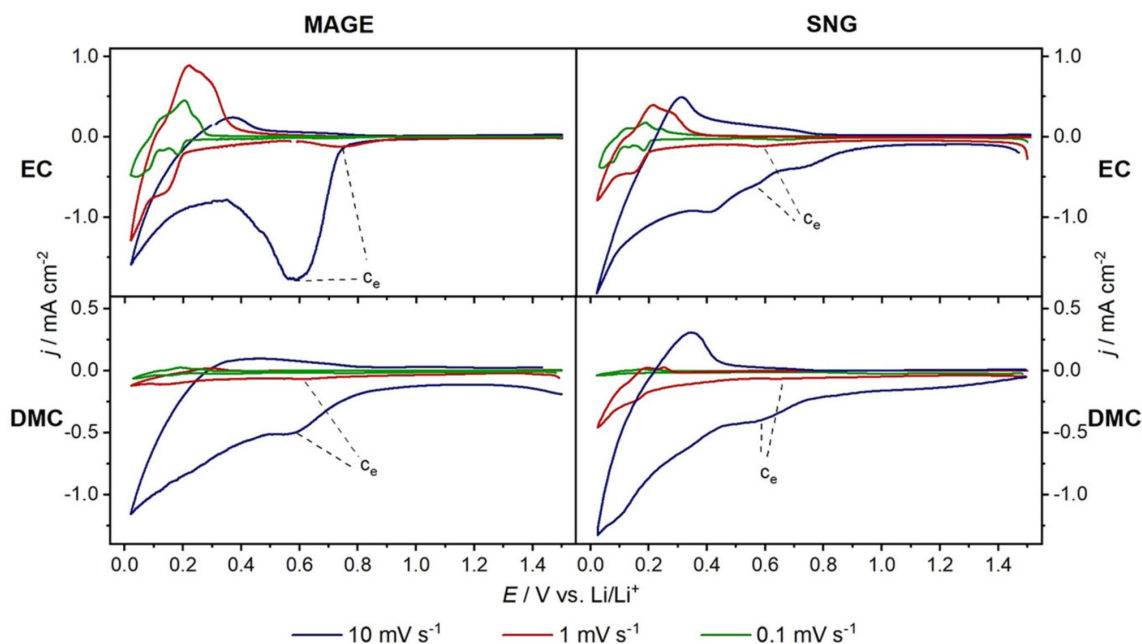


Figure 2. First cycle of the cyclic voltammograms of MAGE (left) and SNG (right) powder film electrodes cycled in EC- (top) and DMC-based (bottom) electrolyte at different scan rates (10, 1 and 0.1 mVs^{-1}).

examining the SEI composition for EC-based electrolyte, the high-potential processes seem to be related to salt decomposition, while reductive solvent decomposition prevails at lower potentials.

Considering the cycling stability, we find a significant loss of current density from the first to the second cycle for all electrode|electrolyte combinations and scan rates (Figure S2). This is both valid for the electrolyte decomposition peak and, to a lesser extent, also for the current density in the Li^+ (de-)intercalation region. The relative loss in the (de-)intercalation region is, however, larger in the DMC-based than in the EC-based electrolyte, likely due to graphite exfoliation. For faster scan rates, we previously reported an activation effect for HOPG electrodes (increasing current densities with continued cycling before passivation sets in).^[33] Based on the present data, this effect seems to be significant only for smooth, basal HOPG substrates where exfoliation may lead to surface roughening. It becomes less important or negligible with increasing defect density of the surface, or when going to powder graphite materials.

Aside from passivating the graphite surface against further electrolyte decomposition, the SEI increasingly modifies Li^+ (de-)intercalation: with continued cycling, the characteristic step-wise Li^+ (de-)intercalation peaks are less resolved. This trend is more pronounced for i) DMC-based than for EC-based electrolyte, and ii) for the samples cycled at fast scan rate (where the peaks are hardly visible even in the first cycle) than for the ones cycled at slow scan rate. The stronger effect in DMC-based single-solvent electrolyte is again attributed to partial graphite exfoliation. The loss in overall current density in the Li^+ (de-)intercalation region upon continued cycling may result either from decreasing Li^+ (de-)intercalation and/or from decreasing electrolyte decomposition, where Li^+ (de-)intercalation at this stage is demonstrated by the respective peak in the anodic scan. Also this loss in current density is more pronounced when cycling in DMC-based electrolyte, due to the partial exfoliation of the graphite materials; and at slow scan rates. In the latter case there is more time for both electrolyte decomposition and graphite exfoliation, leading to a more pronounced loss in current density.

2.1.3. Influence of the Binder

Finally, we also tested the influence of the binder on the electrochemical characteristics of the MAGE and SNG graphite powder film electrodes, using polyvinylidene difluoride (PVDF)-containing electrodes coated onto a Cu foil (see Experimental). Here, we compared the electrochemical characteristics of binder-free graphite powder film electrodes on GC and of PVDF-containing electrodes in commercial LP30 (EC/DMC 1:1 v/v + 1 M LiPF_6) electrolyte. The resulting voltammograms, as well as a detailed discussion of the results, are presented in the Supporting Information (Figure S3 and S4). Even when considering the different experimental parameters, they demonstrate that the electrochemical properties of graphite electrodes cycled in LP30 are dominated by the EC component, which

leads to the formation of a cover layer that passivates against electrolyte decomposition and graphite exfoliation already in the first cycle, while Li^+ (de-)intercalation is still possible. Furthermore, the use of the PVDF binder in the graphite powder electrode has little effect on the formation of this SEI layer and on the Li^+ (de-)intercalation, except for an overall increase in current density.

2.2. Chemical Composition of the SEI: Ex Situ XPS Characterization

Next, we characterized the surface composition of the SEI by XPS to gain further information on the nature of the electrolyte decomposition products. We used depth profiling by Ar^+ ion sputtering to be sensitive not only to the decomposition products formed on the surface of the SEI (sputter time $t=0$), i.e., at the SEI|electrolyte interface, but also to the SEI composition in deeper layers closer to the electrode. The SEI-covered electrode was sputtered for two, four, six and 18 minutes before recording XP spectra, resulting in total sputter times of two, six, 12 and 30 minutes ($t=2$, $t=6$, $t=12$ and $t=30$). Since the samples cycled in DMC-based electrolyte exhibited considerable differential charging effects – evident from broadened peak shapes and arbitrarily shifted binding energies – we will discuss only data obtained on MAGE and SNG electrodes cycled in EC-based electrolyte both at 0.1 and at 10 mVs^{-1} .

2.2.1. Depth-Dependent Elemental Composition of the SEI

Before discussing the spectra in detail, we will summarize the elemental composition (Li, C, O, F, and P) of the SEI layers formed on the MAGE and SNG electrodes at fast and slow scan rates (10 and 0.1 mVs^{-1}), which are derived from the respective signal intensities using the atomic sensitivity factors (ASFs, see Table S1) without any ambiguities arising from peak fitting and deconvolution processes. The evolution of the different elemental concentrations with increasing sputter times is illustrated schematically in Figure 3. Here, it should be noted that the electrolytes used in this study are the same as those employed in a previous study on HOPG electrodes,^[33] which means that differences in SEI formation must be due to structural effects and cannot be caused by electrolyte impurity effects.

F shows concentrations of 8 and 14 at.% on the initial surface of the SEI formed at fast scan rate on the MAGE and SNG electrodes, respectively. Since the Li concentration (17 and 21 at.%) is significantly higher, this results in an excess of Li for these samples, as compared to the 1:1 ratio expected for LiF . The F content is significantly higher after slow cycling, with 30 (33) at.% for the MAGE (SNG) electrode, and the Li content is either slightly lower (MAGE) or identical (SNG) to the F content. For the SEI resulting upon slow cycling, the Li:F ratio already points to a large contribution of species with a 1:1 stoichiometric ratio of both elements, such as LiF (see below). After two minutes of sputtering, the atomic F concentration increases for

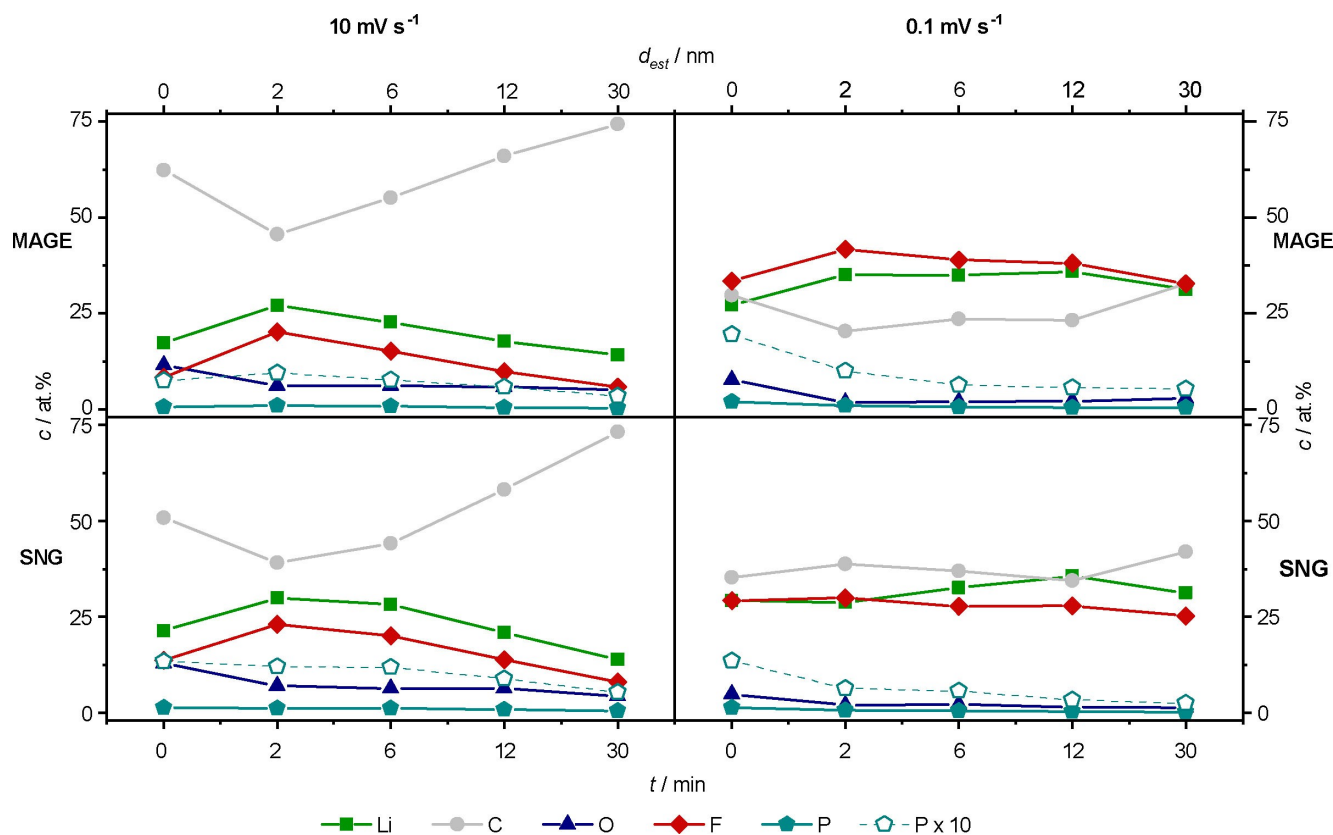


Figure 3. Depth profiles of the elemental composition of the SEI formed on MAGE (top) and SNG (bottom) film electrodes in EC-based electrolyte after cycling at scan rates of 10 (left) and 0.1 mV s^{-1} (right). An estimate of the thickness of the removed SEI layer (d_{est}), starting at the initial SEI surface, is given in the additional upper x-scale.

both electrodes on the SEI obtained after fast cycling, followed by a continuous decrease for the remaining sputtering time. Finally, it reaches 6–8 at.% after 30 minutes sputtering for either of the two electrodes.

The atomic concentration of Li, albeit significantly higher than that of F, follows the trend of the F concentration, increasing between $t=0$ and $t=2$ and decreasing from there on. After 30 minutes, the concentration is around 14 at.% for both electrodes. At slow scan rates, the concentrations of Li and F remain more or less constant (around 30 at.%) for both the electrodes throughout the entire sputtering time. The Li and F concentrations for the graphite powder electrodes cycled both at fast and at slow scan rate are lower than those obtained for the SEI formed on HOPG|EC,^[33] where Li and F were the dominant elements also at fast scan rate, regardless of the electrolyte composition. At the same time, the depth variations for both elements and the close-to 1:1 ratio agree with the trends in the elemental composition of the SEI formed on basal HOPG.^[33]

Focusing on the C concentration, the MAGE and SNG electrodes cycled at 10 mV s^{-1} exhibit high initial concentrations of 62 and 51 at.%, respectively, which is much more than on HOPG. Upon sputtering, the C content varies opposite to the trend observed for F and Li, with an initial decrease to 40–46 at.% after two minutes of sputtering, followed by an increase for longer sputtering times. The latter increase would

be consistent with an SEI composition that is increasingly dominated by solvent decomposition products when going closer to the electrode surface. For the slow scan rate, the C concentration begins at 30–35 at.% for both electrodes, with a small (but still resolvable) initial decrease and subsequent increase for MAGE during sputtering and a more or less constant value for the SNG electrode. Again, this reflects the trends in the Li and F concentrations on these electrodes. Hence, in this case salt decomposition products are dominant in the SEI range probed. A generally similar behavior, with an initial decrease in C concentration followed by an increase/constant value for longer sputter times, was reported for the SEI formed on HOPG electrodes during fast/slow cycling in EC-based electrolyte, albeit with significantly lower C concentrations.^[33] The initial decrease in carbon concentration observed for all electrodes would be consistent with a thin, carbon-rich cover layer, which will be discussed in more detail later. Finally, we would like to note that the more or less pronounced increase in C concentration at the end of the sputtering phase may also indicate that the graphite substrate is reached, similar to our observations for SEI formation on HOPG.^[33] We will demonstrate that this is not the case and that the increase in C concentration mainly results from a different carbon species in the following section.

O represents the second-smallest contribution to the elemental composition of the SEI, with an initial atomic

concentration of about 12 at.% after fast cycling and a lower concentration of 5 and 8 at.% for SNG and MAGE, respectively after slow cycling. This mirrors the scan rate dependence observed for the C concentrations. After two minutes of sputtering, the O concentration decreases and then remains more or less constant for the remaining sputtering time for all electrode materials and scan rates. The lower concentration of O-containing species in the SEI for the samples cycled at lower scan rate, as compared to the values obtained for fast cycling, is in agreement with a preferential solvent decomposition process at fast scan rates, while salt decomposition is more dominant at slow scan rates. This will be discussed in more detail at the end of the next section. The initial decrease in O-content and its later about-constant value also agree with our previous observations for SEI formation on HOPG in the same electrolyte, though the initial oxygen concentration on the latter samples (7–8 at.% for both scan rates) was slightly lower (fast scan) or about equal (slow scan) than on the graphite powder electrodes.^[33]

The smallest contribution, finally, comes from P-containing moieties, whose concentrations are in the range <2 at.% on both MAGE and SNG and at both scan rates. First of all, this reflects the low P concentration in the electrolyte (P:F in LiPF₆ 1:6). The observation of relative P concentrations well below the PF₆ stoichiometry points towards the formation of volatile or soluble P-containing moieties with lower F content during cycling, in addition to LiF formation, leaving P-rich species in the SEI. Based on the relative P 2p intensity, the overall concentration of P-containing moieties arising from salt decomposition is slightly higher on the SEIs formed at 0.1 mVs⁻¹ than on those generated at 10 mVs⁻¹, which agrees with the trends in the F- and O-/C-containing decomposition products. Upon sputtering, the P concentration decays further: for all samples, we find a continuous decrease upon sputtering, with a somewhat steeper initial decay at slow scan rates. For comparison, a steeper decay was observed for the SEI on HOPG electrodes for both scan rates.^[33]

Our data seem to disagree with previous findings from the Peled group.^[40,53] Similar to our observations for SEI formation on the present graphite electrodes cycled at fast scan rates, these authors determined C-containing, organic components from solvent decomposition as dominant species, but for the SEI formed on HOPG during charge/discharge in LiAsF₆-containing EC/DEC (diethyl carbonate) electrolyte. In addition, their result of dominant LiF formation on cross-sectional HOPG is rather similar to our previous findings on basal HOPG, where this prevailed independent of the scan rate.^[33,40]

As stated earlier, these discrepancies may well arise from the very different experimental conditions in our three-electrode half-cell, cyclic voltammetry measurements and in their charge/discharge two-electrode setup.^[33] For instance, we also observe preferential LiF formation on the present graphite powder electrodes at slow scan rate, which would agree with their findings for cross-sectional graphite, i.e., for the more defective carbon materials. Furthermore, these authors also compared the SEI layer formed on so-called “soft” (graphite-like) and on “hard” (non-graphitized) carbon in LiPF₆-containing

EC/DEC electrolyte during charge/discharge measurements. The elemental composition profiles reported by them on the graphite-like carbon are rather close to our present results on the graphite electrodes, except for slightly higher F and slightly lower Li concentrations.^[53]

Overall, our data point to an SEI formation mechanism where salt decomposition is favored at slower scan rates, resulting in higher concentrations of F-containing species (e.g., LiF) within the SEI, while solvent decomposition with predominantly organic, C-containing products is the dominant process at fast scan rates (see also next section). This is different from SEI formation on HOPG in identical electrolytes, where the effect of the scan rate was much less pronounced and high Li and F contents prevailed at both scan rates.^[33]

2.2.2. SEI Compound Identification

In Figures 4 and 5, we present XP detail spectra recorded on the as-prepared SEI layer ($t=0$) and after six minutes of sputtering ($t=6$) of the samples which were cycled at slow scan rate (0.1 mVs⁻¹) in EC (Figure 4: O 1s region and F 1s region, Figure 5: Li 1s, P 2p and C 1s region). Similar spectra recorded after the other sputter times ($t=2$, $t=12$, $t=30$) or from the samples cycled at fast scan rate (10 mVs⁻¹) at all sputter times are presented in Figures S5–S8 and Figures S9–14 in the Supporting Information, respectively. In the following, we will start with the discussion of the components contributing to the elemental peaks in the spectra recorded on the original SEI after subsequent electrode transfer ($t=0$), which were identified by a comprehensive peak fitting and deconvolution procedure. We will also discuss changes in the spectra observed upon sequential sputtering. Finally, we will summarize the evolution of the concentration of different compounds with increasing sputter time (Figure 6). This is closely related to the depth profiles in Figure 3, with the difference that Figure 6 displays the concentration profiles of different compounds or moieties rather than elemental profiles. Finally, we will try to rationalize these results in a mechanistic picture, which can explain in particular the effects of scan rate, substrate and electrolyte. Here, we will include also transport effects, which have been discussed in previous experimental and theoretical studies.^[25,54,55]

For the identification of the different compounds contributing to the SEI and their relative contribution, we applied a comprehensive procedure for XPS peak fitting which has been recently employed for the analysis of similar SEI films on HOPG model electrodes.^[33] In short, it is based on the following assumptions: 1) the number of possible components is restricted to a minimum, 2) the binding energies (BEs) and the peak widths (full width at half maximum – FWHM) of the elemental peaks of a given component are fixed to ± 0.2 eV for all spectra (different electrodes, different scan rates) at $t=0$, and 3) except for the cases indicated, the intensities of the elemental peaks related to a given compound reflect the stoichiometry of that compound, corrected by the atomic sensitivity factors (ASFs). The contribution of the respective

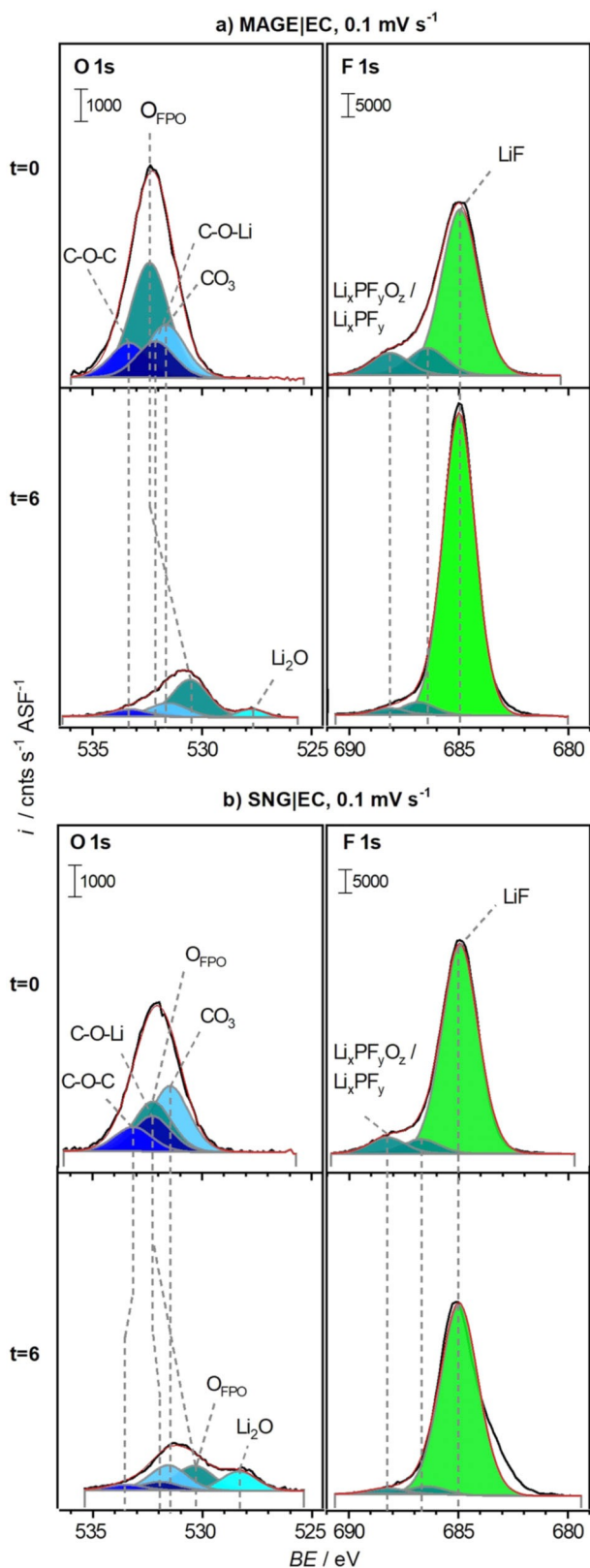


Figure 4. XP detail spectra of the O 1s and the F 1s regions of the SEI formed on a) MAGE and b) SNG powder film electrodes cycled at 0.1 mV s^{-1} on the as-prepared samples ($t = 0$) and on the samples obtained after six minutes of sputtering ($t = 6$). The red lines indicate the sum of the individual peak intensities.

compounds or moieties is calculated from the sum of the individual elemental contributions, which means that only contributions from C, F, Li, O and P are included. For moieties with unknown composition, such as the fluorophosphates Li_xPF_y or $\text{Li}_x\text{PF}_y\text{O}_z$, the compound concentration was calculated from the intensities of the respective peaks with appropriate BEs. The concentrations of these species were limited to the sevenfold of the P concentration at maximum, reflecting the stoichiometry of the undecomposed compound with the highest O and F content, e.g. LiPF_6 , while lower concentrations, arising from lower O and F contents due to sputter-induced decomposition, were possible. The different components considered were mainly derived from previous studies, including our own.^[33,40,53,56–59] Further details are given in the Supporting Information of Ref. [33]. We believe that this is the most rational approach for a consistent fit of all elemental peaks, even though some of the individual fits may not be perfect. The BEs and stoichiometric ratios used for peak fitting and quantification are listed in Table 1. Note that a slight peak broadening and shift occurs upon sputtering.

Beginning with the F 1s, we find a pronounced signal at 685.0 eV (Figure 4 and S10), which can be related to LiF (see discussion of the Li 1s peak),^[60] and two smaller signals at higher binding energies (686.6 and 688.3 eV), which are assigned to $\text{Li}_x\text{PF}_y\text{O}_z$ and Li_xPF_y species (no fixed stoichiometries), respectively.^[33,48,61]

The amount of LiF is about 50 at.% after slow cycling and about 10–25% for the samples cycled at fast scan rate (see Figure 6). The at.% values given for (stoichiometric) compounds are the sums of the contributing elemental values. This value of 50 at.% is significantly less than the 70 to 80 at.% which we had detected in the SEI formed on basal HOPG electrodes, independent of the scan rate.^[33]

Also, the concentration of the other F-containing species ($\text{Li}_x\text{PF}_y\text{O}_z/\text{Li}_x\text{PF}_y$) is higher after slow cycling (0.1 mV s^{-1}) than the one obtained after fast cycling (4–8 at.% vs. 2 at.%). This observation is in line with findings reported by Ryu *et al.*, who studied the SEI formation in EC/DEC-based Li^+ -containing electrolyte with different anions on 'graphite bulk'.^[56] Comparing the CVs in different electrolytes, they could distinguish between salt (anion) and solvent decomposition, where salt decomposition occurred at different potentials depending on the anion. For LiPF_6 , these authors found a distinct peak at higher potentials than solvent decomposition, which was claimed to proceed with an exponentially increasing rate at lower potentials.

Based on these observations, the effect of the scan rate in our experiments can be explained by different potential dependencies of the two competing decomposition processes, in combination with kinetic limitations, e.g., in the formation of the passivation layer. In this case, cycling at slow scan rates would favor the build-up of a passivation layer via the process with the earlier onset in the negative-going scan (thermodynamically favored, salt decomposition) over the process with the steeper increase with increasing overpotential (kinetically favored, solvent decomposition). Cycling at higher scan rate, in contrast, would be more affected by kinetic limitations and thus

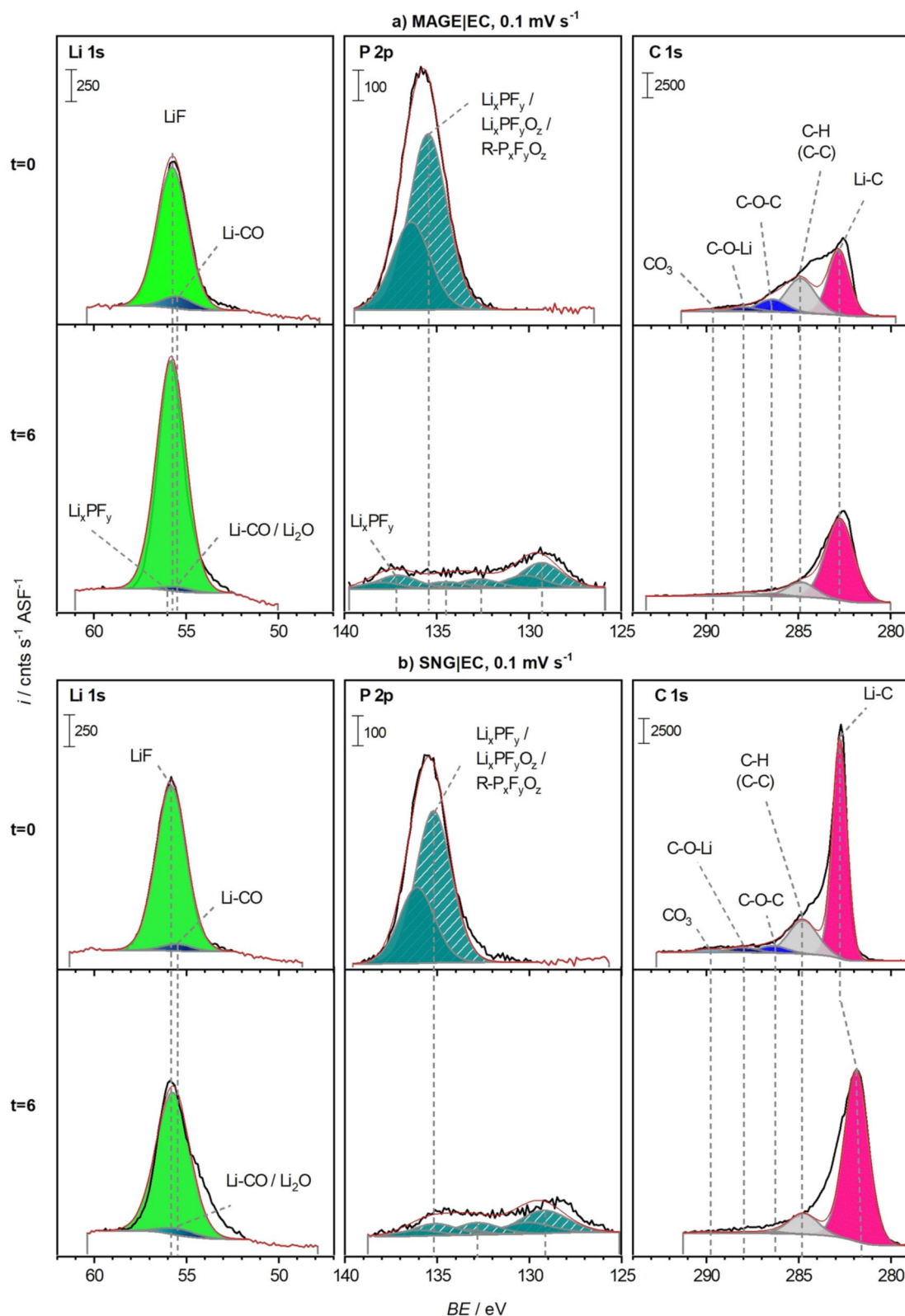


Figure 5. XP detail spectra of the Li 1s, P 2p and the C 1s regions of the SEI formed on a) MAGE and b) SNG powder film electrodes cycled at 0.1 mV s⁻¹ on the as-prepared samples (t = 0) and on the samples obtained after six minutes of sputtering (t = 6). The red lines indicate the sum of the individual peak intensities.

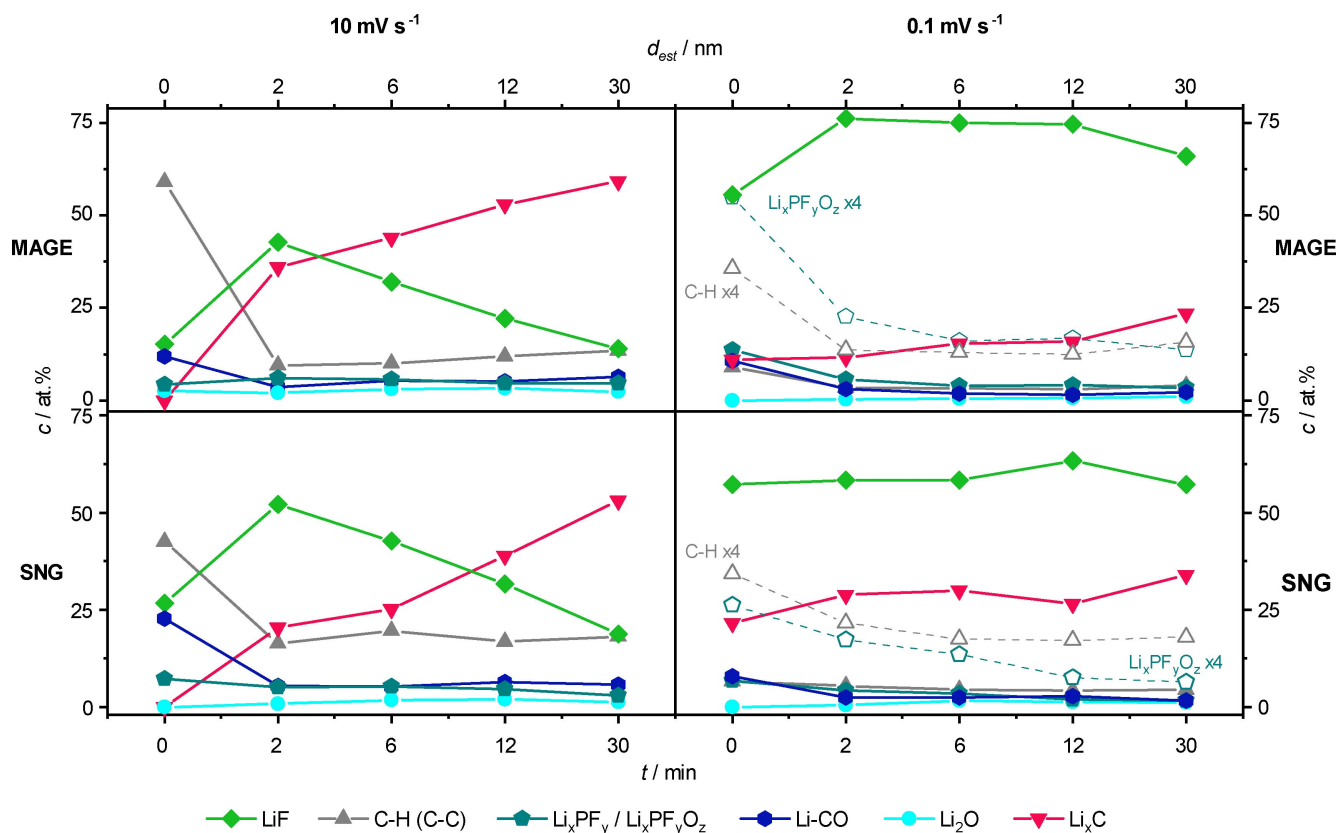


Figure 6. Depth profiles of the XPS-probed concentrations of selected species on MAGE (top) and SNG (bottom) graphite electrodes cycled at 10 (left) and 0.1 mV s^{-1} (right). The concentrations are given in at.%. For the calculations, we only used the elemental concentrations of C, F, Li, O, and P. The open symbols connected by broken lines represent up-scaled versions of the C-H and P-containing species, included for better comparison. An estimate of the thickness of the removed SEI layer (d_{est}), starting at the initial SEI surface, is given in the additional upper x-scale.

	C 1s [eV]	O 1s [eV]	Li 1s [eV]	F 1s [eV]	P 2p [eV]	Ref.
C–O–C (polymer/ether) (2)	286.4	533.3 (1)				[57], [62] [63]
C–O–Li (alkoxide) (1)	288.0	532.1 (1)	55.5 (1)			[58], [66]
Li ₂ CO ₃ (carbonate)	290.0	531.7	55.5			[14], [60]
LiF			55.8	685.0		[60]
Li _x PF _y O _z / R–P _x F _y O _z		~532 upon sputtering: ~530		686.6/688.3	Fast: 134.0, 136.7 Slow: 134.5/135.2 upon sputtering: 132.8/129.4	[48], [59]
LiPF ₆			56.0	687.5	137.6	[17], [61]
Li ₂ O		~528	55.5			[66]
LiOH		~531				[60]
C–H (C–C)	~285					[60]
Li _x C	~283		55.5			[67]

emphasize the kinetically preferred solvent decomposition. Possible reasons for such behavior will be discussed at the end of this section.

Upon short sputtering ($t = 2$), the LiF concentration increases for all electrodes and scan rates, except for the SNG | EC sample cycled at 0.1 mV s^{-1} , where it remains about constant. On the other hand, the combined contribution of the two

signals related to Li_xPF_yO_z and Li_xPF_y decreases continuously, also for longer sputtering times, and in some cases even disappears completely (see Figures S10, S12 and S14). While this behavior is likely to reflect the concentration profile of these species, we cannot rule out that their decreasing concentration is due to increasing sputter decomposition of the Li_xPF_yO_z and Li_xPF_y species, or a combination of both.

In the O 1s region, we identified peaks at 533.3, 532.1 and at 531.7 eV, which can be correlated to specific C 1s signals. These O 1s peaks have been assigned to polymer, ether or semicarbonate species ($\text{C}-\underline{\text{O}}-\text{C}$ or $\text{R}-\text{C}-\underline{\text{O}}-\text{CO}_2^-$) at 533.3 eV,^[57,62,63] to alkoxide species ($\text{C}-\underline{\text{O}}-\text{Li}$)^[58] at 532.1 eV, and finally to semicarbonate species ($\text{R}-\text{C}-\text{O}-\underline{\text{CO}}_2^-$)^[64] or Li_2CO_3 ^[14] at 531.7 eV. (Note that the authors of a recent study claimed that the semicarbonate is actually lithium ethylene monocarbonate (LiEMC).^[65]) As will be shown later, contributions from such semicarbonates seem to be negligible in our case. Interestingly, Li_2CO_3 was not observed in the SEI formed on HOPG.^[33] This discrepancy may arise from the lower defect density of the basal HOPG substrate, which could affect the SEI formation. The combined amount of carbonates, alkoxides and polymer or ether species, which we consider as typical solvent decomposition products, is about similar on all electrodes, except for the MAGE anode cycled at 10 mVs^{-1} . The lower concentration of these species on the latter electrode agrees well with the absence of a C 1s peak in the range of 290 eV (see below), which is typical for carbonates, and the related O 1s component on that electrode. In addition to the aforementioned O-containing species, two further O 1s peaks are required for a reasonable fit. An O 1s signal at about 532 eV ($t=0$) is tentatively assigned to fluorophosphates, e.g., $\text{Li}_x\text{PF}_y\text{O}_z$ (labelled O_{PFO}), based on the fact that we also observe a P 2p signal with a BE typical for these species (see below).^[61] For the MAGE samples, this component contributes most to the O 1s signal, both for the graphite electrodes cycled at 0.1 and 10 mVs^{-1} , while its contribution is smaller (second highest) for the SEI surface formed on SNG anodes. Note that the O 1s signal at $\sim 532 \text{ eV}$ may also contain contributions from simple inorganic components, such as Li hydroxides ($\sim 531.0 \text{ eV}$)^[60], which may form by reaction with residual moisture in our solvents ($< 50 \text{ ppm}$). This may lead to a too-high content of these species in the calculations (see Figure 6), which is at least partly corrected by limiting the content of these species to the sevenfold of the P-concentration. The Li 1s signal would not be in disagreement with that possibility. Finally, we detected a small signal at 528.4 eV in the O 1s spectrum of MAGE cycled at 10 mVs^{-1} , which, based on its BE, is most likely related to Li_2O .^[66] This may result, e.g., from side reactions of Li_2CO_3 with trace impurities of water or from sputter decomposition of Li_2CO_3 .^[66] For the spectrum recorded before Ar^+ sputtering ($t=0$), however, the latter origin can be excluded. Since for this sample there was also no carbonate signal at 531.7 eV at $t=0$, this seems to indicate that the carbonate species on that surface reacted chemically to Li_2O , either via side reactions or during the cleaning process. It is important to note that a number of peaks seemed to shift in BE upon sputtering. Consequently, an unambiguous assignment is often hard to make. In these cases we tried to maximize the number of peaks with constant BE. For the other three samples (SNG | EC at fast and slow scan rate, MAGE | EC at slow scan rate), the Li_2O -related signal around 527–528 eV appeared only after two minutes of sputtering. In this case, it may also originate from sputter decay of Li_2CO_3 and semi-carbonates or from solvent decomposition due to reaction with traces of water.^[33,66]

Among the three C- and O-containing species identified in the O 1s region (polymer/ethers, carbonates and alkoxides), carbonates have the highest concentration based on their O 1s intensity, except for the MAGE | EC sample cycled at 10 mVs^{-1} , where this species does not appear at all. This latter sample also suffers most upon sputtering. The $\text{Li}_x\text{PF}_y\text{O}_z$ -related O 1s signal (O_{PFO} , $\sim 532 \text{ eV}$) decreased during sputtering; simultaneously, a signal appeared at lower binding energies ($\sim 530 \text{ eV}$). The latter peak may reflect the presence of organophosphates with lower P oxidation states ($\text{R}-\text{P}_x\text{F}_y\text{O}_z$), which are observed in the P 2p signal (see also discussion below).^[59] In contrast to the decreasing concentration of F species for higher scan rates, the overall concentration of O-containing species increases with faster scan rate. This can be explained in the same picture as before, with a dominant SEI formation from decomposition products of the Li salt (mainly LiF) at slow scan rates, while solvent decomposition products (i.e., C- and O-containing compounds) contribute more strongly to the SEI formation at fast scan rates.

In order to fit the experimental data in the C 1s region, we started with the components derived from the O 1s detail spectra, including polymer / ether ($\text{C}-\text{O}-\text{C}$, e.g., polyethylene oxide (PEO)^[57,62] or (semi-)carbonate ($\text{R}-\underline{\text{C}}-\text{O}-\text{CO}_2^-$)^[63]) species at 286.4 eV, alkoxides ($\text{C}-\text{O}-\text{Li}$, 288.0 eV)^[58] and (semi-)carbonate (CO_3^{2-} or $\text{R}-\text{C}-\text{O}-\underline{\text{CO}}_2^-$, 290.0 eV)^[63] species. Where unclear, the stoichiometries (C:O ratios) of the above components are listed in Table 1. Based on the rather low intensity in the O 1s region at 533.3 eV, the formation of significant amounts of semicarbonates with a C(286.4 eV) : O(533.3 eV) ratio of 1:1 can be excluded. Therefore, the C 1s peak at 286.4 eV must be mainly due to polymer and ether species. Accordingly, the C 1s peak at 290.0 eV is mainly assigned to Li_2CO_3 . This is compatible also with the O 1s intensity at 531.7 eV, which fits to a C:O ratio of 1:3 for the related peaks. The absence of semicarbonates seems to be in contradiction with the findings of Cresce *et al.*, who observed a 1:1 ratio between the C 1s signals at $\sim 290 \text{ eV}$ and 286.8 eV, respectively, on their HOPG samples before rinsing, which is typical for semicarbonate.^[39] After thorough rinsing, however, they obtained much higher carbonate concentrations compared to semicarbonates. Since our XPS measurements were performed after extensive rinsing, both experiments arrive at the same result of a low semicarbonate concentration on the well-rinsed SEI. Furthermore, we find significant contributions from a C 1s signal for adventitious carbon / hydrocarbon groups ($\text{C}-\text{H}/\text{C}-\text{C}$) at approximately 285 eV,^[60] which appears for all electrode | electrolyte combinations and both scan rates.

While these peaks lead to very reasonable fits for both electrodes directly after cycling at 10 mVs^{-1} ($t=0$), an additional signal is required at 282.7 eV ($\text{Li}-\text{C}$, FWHM 0.9–1.2 eV at $t=0$) for the SEI formed upon cycling at 0.1 mVs^{-1} . In our previous study on HOPG model electrodes, we observed a peak at approximately 283 eV after sputtering. We had attributed this signal to Li carbide species (Li_xC)^[67] which were generated upon sputtering.^[33] Since, in the present study, this signal appears already before sputtering, this carbide species must (also) be formed in the (electro-)chemical decomposition

process during the slow CV measurements rather than only by sputter-induced decomposition. Apparently, this chemical process is enhanced on rough surfaces, since the peak did not appear in the equivalent measurements on HOPG.^[33] For the present electrodes, this species contributes significantly to the SEI composition (see Figure 6), which will be discussed in more detail later. It is important to note that the increasing C 1s intensity in the last sputter cycle (see Figure 3) is mainly due to an increase of this Li carbide species and not caused by an upcoming signal of graphite electrode material, which should be at 284.6 eV. This assignment is further supported by the fact that the different C 1s signal intensities are still changing even at later stages. While it is reasonable to expect that SEI constituents are present in the inner pores of the electrode and thus can be observed also after removal of the surface SEI layer, one would not expect changes in the composition in that case. Hence, we can reasonably exclude that the graphite electrode is unburied during 30 minutes of sputtering, which also means that the SEIs formed on these graphite electrodes are significantly thicker than those formed on HOPG.^[33] Finally, we would like to note that there is additional intensity in the range between the C–H/C–C signal at 284.8 eV and the Li_xC signal at 282.7 eV in the spectra of the samples cycled at slow scan rates. We think that this results from Li-containing carbon species with lower Li content, which therefore appear at higher BEs. Because of the unknown nature of these species, however, we did not include an additional peak for them. In agreement with the trend in the O 1s intensities of the O- and C-containing species, the overall carbon concentration of C-containing species is higher after cycling at 10 than after cycling at 0.1 mVs⁻¹. This is again compatible with a mechanism favoring more pronounced solvent decomposition at faster scan rates, while salt decomposition prevails at slow scan rates.

For the P 2p signal, which consists of a doublet with a spin-orbit separation of $\Delta 0.9$ eV, we resolve a p_{3/2} signal at 136.7 eV and another one at about 134.0–134.4 eV for $t=0$ after fast cycling (10 mVs⁻¹), which we assign to LiPF₆ and its decomposition products, e.g., Li_xPF_y and Li_xPF_yO_z.^[48,61] After slow cycling (0.1 mVs⁻¹), the P 2p spectrum at $t=0$ consists of a single signal only at 134.5 eV for MAGE and at 135.2 eV for SNG, respectively. We attribute these BEs to different compositions of the Li_xPF_y and Li_xPF_yO_z species. Accordingly, we did not assume a fixed stoichiometry and therefore the P:F or P:O intensity ratios were allowed to vary freely within certain limits: the concentrations of these species were limited to the sevenfold of the P concentration at maximum. The peak at 136.7 eV observed for the SEI formed at fast scan rate ($t=0$) is tentatively assigned to LiPF₆^[17] which was not removed despite careful rinsing. Sputtering of the electrodes leads to a significant decrease of the P 2p intensities in the Li_xPF_yO_z- and Li_xPF_y-related signals at 134.4–136.7 eV which, in all cases, is accompanied by the appearance of new signals at 132.8 and 129.7 eV. This is particularly well visible in the spectra, e.g., in Figure 5 or Figure S9. We explain this by sputter-induced decomposition of the Li_xPF_yO_z/Li_xPF_y components and the appearance of (organo-)phosphates (R–P_xF_yO_z, see also the O 1s discussion) and phosphides / elemental phosphorous. Interest-

ingly, we observed a weak signal at about 137 eV on the sputtered MAGE electrode which, based on the BE, could be LiPF₆. Also note that the total amount of P decreases in the SEI with increasing sputter time, regardless of the graphite material and the scan rate (see discussion of Figure 3).

Finally, for the Li 1s region, peak fitting resulted in two main peaks at 55.5 eV and 55.8 eV for both anode materials and cycling times. We assign them to LiF (55.8 eV)^[60] and to Li carbonates / alkoxides (55.5 eV), respectively.^[60,66] The latter species, which result from solvent decomposition, are labelled as Li–CO in the spectra. The intensity of the LiF-related Li 1s peak is given by the intensity of the corresponding LiF component in the F 1s spectrum (Li:F ratio of 1:1). The intensity of the Li–CO signal is calculated from the overall amount of Li- and O-containing species, assuming Li:O ratios of 2:3 (for the O 1s component at 531.7 eV) for Li₂CO₃ and of 1:1 (for the O 1s component of alkoxides at 532.1 eV), respectively. Assuming that the high-energy peak of the P 2p spectrum for the SEIs formed at 10 mVs⁻¹ ($t=0$, Figure S9) results from residual, undecomposed LiPF₆, we calculated the intensity of the related Li 1s peak, which appears at 56.0 eV (note that due to the small contribution this is hardly visible). The lower overall amount of Li–CO (alkoxide, carbonate) species obtained for the samples cycled at 0.1 mVs⁻¹ compared to those obtained after fast cycling (10 mVs⁻¹) at $t=0$ (see also Figure 6) reflects the behavior of the respective O and C signals, which were used to calculate the intensity of the respective Li 1s peak.

Figure 6, finally, depicts the evolution of the concentrations of the different SEI constituents (e.g., LiF, Li₂O, Li–CO, Li_xC) and moieties, which are based on the respective concentrations of C, F, Li, O, and P therein in at.%, with increasing sputtering for the respective samples. The term Li–CO is used to summarize contributions from different solvent decomposition products, including carbonates, ethers or polymers and alkoxides. The line labelled C–H (C–C) reflects the contribution from the C 1s signal for hydrocarbon species at ~ 285 eV, which will also include adventitious carbon. The atomic concentrations of these species for all four electrodes and at all sputter times are listed in Table S2 in the Supporting Information. In addition to sensing the depth-dependent concentrations of the various compounds or moieties, these data may also reflect sputter-induced transformations of the original SEI components.

For both graphite materials, LiF represents the highest contribution to the SEI surface formed at slow scan rate and the second-highest contribution at fast scan rate. After two minutes of sputtering, all samples show a significant increase in the LiF concentration, except for SNG | EC (0.1 mVs⁻¹), where the concentration remains more or less constant. Similar to our observations on SEI formation on HOPG in these electrolytes, LiF is one of the two main components within the SEIs. For the samples cycled at slow scan rate, its concentration remains approximately constant after the initial increase throughout the remaining sputtering time, while for those cycled at 10 mVs⁻¹ it passes through a maximum concentration after two minutes of sputtering ($t=2$) and then decreases steadily from thereon (Figure 6). Hence, except for SNG | EC (0.1 mVs⁻¹), the LiF concentration is lower directly at the SEI surface, and then

either increases in the near-surface regions or remains constant, depending on the cycling rate. These results can be compared with previous findings on related systems. For the SEI generated on basal HOPG electrodes under similar conditions we observed a high and approximately constant LiF concentration upon sputtering.^[33] Niehoff *et al.* reported an increase of the LiF concentration upon sputtering, with a maximum after 1–3 minutes, and a subsequent decay for a comparable system (composite electrode, EC/DEC + LiPF₆).^[67] Furthermore, these authors could demonstrate that the increase of the LiF concentration (in at. %) during the first 30 seconds of sputtering correlates quantitatively with the decrease in the Li_xPF_y/Li_xPF_yO_z concentration.^[67]

This is different from our present findings, where sputter-induced decomposition of Li_xPF_y and Li_xPF_yO_z species is likely to occur as well, but, due to their low concentration at $t = 0$, cannot explain the pronounced increase in the LiF concentration observed between $t = 0$ and $t = 2$. Peled and coworkers, in contrast, reported an initial increase of the LiF concentration upon sputtering an SEI that was generated during galvanostatic charge/discharge experiments on cross-sectional HOPG in EC/DEC + LiAsF₆ electrolyte, followed by a constant concentration. For the basal plane, in contrast, they observed a maximum after eight minutes of sputtering and a decay for longer sputter times.^[40,53] We find it most likely that the initial increase in LiF concentration is due to the removal of a thin surface layer of carbon-rich deposits, which may have resulted, e.g., from the after-treatment of the electrode (see the following discussion).

The C–H moieties, which contribute most to the SEI formed on these graphite materials upon cycling at 10 mV s⁻¹, start with an initial contribution of 58 (42) at. % on the MAGE (SNG) sample, which then decreases considerably for both electrodes upon sputtering. After longer sputtering times their contribution passes through a minimum and then increases again for the MAGE electrode (final concentration ~30 at. %). For the SNG electrode, their concentration is about constant (~20 at. %) at longer sputtering times. Upon cycling at 0.1 mV s⁻¹, the initial concentrations are significantly lower (~6 at. % for both MAGE and SNG). They, too, decrease during the initial two-minute-sputtering phase and then remain more or less constant. These results are consistent with a model that involves the presence of a C–H-rich deposit layer on the SEI surface (SEI | electrolyte interface). This will be discussed at the end of this section.

The initial intensities of the combined Li–CO solvent decomposition species are about 12 at. % for the MAGE samples, both after fast and slow cycling, and about 25 (6) at. % for the SNG samples cycled at fast (slow) scan rate. After two minutes of sputtering, the concentration decreases considerably, regardless of the substrate and the cycling rate, and then remains about constant upon longer sputtering. Both this and the similar trend of the C–H species upon sputtering point to an approximately constant concentration of solvent decomposition products throughout the probed SEI, underneath a surface region where these species appear in higher concentrations. The initial decrease agrees with reports by Peled *et al.*^[40,41,53] and Edström *et al.*,^[57,62] who proposed that organic (solvent decomposition) products are enriched at the SEI surface (electro-

lyte | SEI interface). Upon sputtering, these organic species are quickly removed.

The Li_xPF_yO_z/Li_xPF_y signal with its contributions from related P 2p, Li 1s and F 1s signals is the second-lowest contribution to the SEI composition at $t = 0$. It is slightly higher on the MAGE electrodes (13 at. %) than on the SNG electrodes (6–7 at. %), regardless of the scan rate. Sputtering initially causes the concentration of these species to decrease to ~5 at. %, independent of electrode material and scan rates. From thereon, the concentration remains about constant (MAGE) or continues to decrease (SNG). The initial decrease in concentration of this species is attributed to a sputter-induced decomposition to LiF, reflected by the initial increase in LiF concentration. The higher original concentration of Li_xPF_yO_z/Li_xPF_y on the slowly cycled MAGE electrode would fit to the higher overall amount of Li salts after slow cycling.

The Li_xC C 1s signal at about 283 eV appears first after two minutes of sputtering for the samples cycled at fast scan rates, while it is present already before sputtering after slow cycling (see our earlier discussion of the C 1s deconvolution). For the latter samples, the concentration of Li_xC remains about constant during sputtering, while it increases continuously for the fast cycled electrodes, reaching more than 50 at. % for both the MAGE and the SNG electrode. As discussed before, the BE clearly indicates that this signal is not due to contributions from the graphite substrate, as it was observed for HOPG.^[33] This also means that the SEI formed on the graphite powder film electrodes is significantly thicker than that created under identical conditions on HOPG, which is in full agreement with expectations.

Finally, we also observed the formation of Li₂O, which is indicated by the O 1s signal at 528.4 eV and a Li 1s signal at 55.5 eV. In most cases, this species appeared only after sputtering. The only exception was the MAGE electrode cycled at 10 mV s⁻¹, where it was detected also at $t = 0$. During sputtering, its concentration remained below 3 at. % in all cases. We assume that this species results mainly from decomposition of carbonates, either by chemical interaction or upon sputtering.^[66]

Overall, our results are consistent with an SEI formation process where solvent decomposition prevails at fast scan rates, resulting in dominant contributions from solvent decomposition products (Li–CO species). At slow scan rates, salt decomposition is the dominant process, with LiF and Li_xPF_yO_z species as typical decomposition products. This is clearly evident already from the total amount of C or F in the SEI, and thus does not depend on the deconvolution procedure. The more or less pronounced initial increase in LiF concentration upon sputtering, which is also indicated by the total F and Li concentrations, is tentatively explained by effects of the after-treatment (rinsing, sample transport). This can involve both removal of Li salts from the surface region and deposition of a carbon-rich surface layer. The general decrease of the Li salt content with increasing sputtering time, i.e., in deeper layers of the SEI, can be explained by transport effects, which have been reported both in experimental and theoretical studies on SEI formation in LIBs.^[25,55] In the case of a porous SEI which grows

at the electrode surface, the SEI surface reflects the initial SEI at the onset of SEI formation. If the ongoing SEI formation takes place at the electrode surface and is dominated by transport effects, and if transport of Li salts through the growing SEI is more hindered compared to solvent transport, SEI formation at later times would more and more be governed by solvent decomposition. Note that, in this case, differences in the efficiency of SEI formation are also due to differences in the chemical interaction between graphite electrode and solvent molecules. The effect of the scan rate during cycling can be rationalized in the same way, since transport effects should be less pronounced during slow cycling. Hence, one would expect higher salt concentrations at the electrode surface for slow cycling, and the decay of the salt components with increasing thickness of the SEI should be less pronounced. As expected, the effects explained here by hindered transport in the growing SEI are much less pronounced in the thinner SEI layers observed on HOPG. These effects should depend also on the transport properties of the solvent molecules, which are not so different in the present case, and the pore structure of the SEI. Focusing on the $\text{Li}_x\text{PF}_y\text{O}_z$ species, which can be considered as intermediates in the formation of LiF, their low concentration compared to LiF indicates that these rapidly decompose to LiF during cycling. In addition, their decomposition seems to be induced also by Ar^+ sputtering, which results in a distinct decay after the first sputter cycle. The amount of carbon-containing solvent decomposition products increases when approaching the electrode surface, mirroring the decreasing amount of salt decomposition products. This trend is more pronounced for the SEI created by fast cycling. Similar to LiPF_6 decomposition to $\text{Li}_x\text{PF}_y\text{O}_z$ and LiF, we find two groups of decomposition products; C–C/C–H and Li_xC species. Sputter-induced decomposition processes play a role in this case, as well: the increasing concentration of Li_xC species, relative to the total amount of carbon, reflects the increasing decomposition of C–C/C–H species by Ar^+ sputtering. Nevertheless, there must be a pathway for purely electrochemical formation of the carbide species from solvent decomposition products during cycling as well, since these species are observed also on the initial surface of the SEI formed after slow cycling.

Finally, we would like to note that in the present case we concentrated on the transport of solvent molecules and salt species. Transport of Li^+ ions, which must be active to allow Li^+ (de-)intercalation and cell currents under conditions where further SEI formation is negligible, was not considered. Nevertheless, this simple model can explain our findings on the SEI composition and its variation rather well on a qualitative scale.

3. Conclusion

Extending our previous study on SEI formation in LiPF_6 -containing single-solvent carbonate electrolytes on structurally well-defined HOPG electrodes, we have investigated this process on more realistic binder-free and binder-containing graphite powder film electrodes by cyclic voltammetry and chemical analysis of the SEI by depth profile XPS. Binder-free

electrodes were prepared using two different types of graphite, an artificial commercial graphite powder (MAGE) and a spheroidised natural graphite (SNG). For comparison, also binder-containing electrodes prepared from these graphite materials were studied. Employing different potential scan rates and two different LiPF_6 -containing single-solvent (EC and DMC) electrolytes, as well as the commonly used LP30 electrolyte (EC + DMC), we arrive at the following main results and conclusions:

1. Despite of their different nature and particle size, the two graphite materials are rather similar in their electrochemical properties in the single-solvent electrolytes, both with respect to electrolyte decomposition and Li^+ (de-)intercalation. Compared to the HOPG model electrodes, the LiF content in the SEI is generally lower and the SEI formed during cycling is thicker. The addition of a binder has some effect on the electrochemical properties in LP30: most prominently, it shifts the electrolyte decomposition to more negative potentials compared to binder-free electrodes. The pronounced peak-broadening observed on these electrodes is mainly attributed to transport effects and inhomogeneities in these thicker electrode layers.
2. In contrast to the limited influence of the nature of the graphite powder, the nature of the electrolyte and the scan rate during potential cycling have a (more) pronounced effect on the SEI formation and its composition on these electrodes. For DMC-based electrolyte, the SEI formation is less efficient and probably results in – at least partial – graphite exfoliation, allowing further electrolyte decomposition even in the third cycle. When cycling in EC-based electrolyte, in comparison, electrolyte decomposition and thus further SEI formation are negligible after the first cycle. This is attributed to differences in the chemical interaction between graphite electrode and solvent molecules. The characteristic features for electrolyte decomposition and Li^+ (de-)intercalation are, however, comparable in both cases, except for a slight difference in the peak positions. In LP30, the more efficient EC decomposition seems to dominate the solvent decomposition process.
3. The effect of the scan rate is most pronounced. It severely affects the composition of the resulting SEI and causes variations in the composition when going towards the SEI|electrode interface. Fast cycling results in a generally lower concentration of salt decomposition products and a continued distinct decrease of their contribution with increasing depth, while the content of salt decomposition products is much higher and changes with increasing depth are much less pronounced for the SEI formed at slow cycling. The concentration of carbon-containing salt decomposition products mirrors these trends. These distinct variations and trends are explained in terms of transport limitations, where SEI formation takes place directly at the electrode surface and transport of salt species through the growing SEI layer is more hindered than transport of solvent molecules. This effect increases with increasing thickness of the SEI. The competition between salt transport and ion transport through the growing SEI is likely to be affected also by the

transport properties of the solvent molecules and by the pore structure of the SEI.

Overall, these results and their comparison with previous findings on SEI formation under similar conditions and in similar electrolyte, but on structurally well-defined HOPG electrodes, provided detailed insights into the SEI formation process and the underlying mechanisms, including transport effects, which will be useful for further systematic studies and the improvement of the SEI.

Experimental Section

Graphite powder film electrodes were prepared from aqueous suspensions (4 mg ml⁻¹) of commercial MAGE graphite (Hitachi Chemical Co., Ltd.) and spheroidized natural graphite powder (SNG) modified by the Zentrum für Sonnenenergie- und Wasserstoff-Forschung Baden-Württemberg (ZSW), respectively. The binder-free electrodes were prepared by depositing 50 µl of the sonicated graphite solution on a polished glassy carbon electrode (diameter 8 mm, mass loading: 0.4 mg cm⁻²), which were then dried under a N₂ stream. For the binder-containing electrodes (see also Supporting Information), a thin film of a graphite ink, consisting of the respective graphite powder (MAGE or SNG) and polyvinylidene difluoride binder (PVDF, Solvay) in N-methylpyrrolidone (NMP, Sigma Aldrich, 99.5%) was homogenized, coated onto a dendritic Cu foil (Schlenck Metallfolien) by doctorblading, and finally dried at 40 °C (2 hrs) and 60 °C (4 hrs) (approximate mass loading 3.5 mg cm⁻²). The ink was prepared by adding an 8 wt.% solution of PVDF in NMP to the graphite material to reach a graphite : PVDF ratio of 95 : 5.

Structural characterization of the graphite powders was conducted via transmission electron microscopy (TEM) using a JEOL1400 bright-field transmission electron microscope (BF-TEM) equipped with a CCD camera (electron energy 90 keV). For imaging, a droplet of ethanol (Merck Emsure) containing the graphite powder (ca. 1 mg ml⁻¹) was pipetted on a carbonized copper grid (Plano, Mesh 300) and transferred to the microscope after evaporation of the solvent.

For the electrochemical measurements, we used either 1 M solutions of LiPF₆ (Sigma Aldrich, battery grade/99.99 + %) in ethylene carbonate (EC, Sigma Aldrich, 99.5%, ≤ 50 ppm H₂O) or in dimethyl carbonate (DMC, Sigma Aldrich, 99.0%, ≤ 20 ppm H₂O) as electrolytes, which were prepared by mixing the salt into the respective solvents and stirring for 45 minutes. EC, which is solid at room temperature, was warmed to 65 °C, mixed with LiPF₆ and stirred while cooling.^[33] It remained liquid for at least 48 hrs. For the comparative measurements of binder-free and binder-containing electrodes, LP30 (1 M LiPF₆ in EC/DMC, 1:1 v/v, Solvionic, 99.9%, ≤ 20 ppm H₂O) was employed as electrolyte. The electrochemical measurements were performed in an open Kel-F beaker cell with an electrolyte volume of 0.3 ml for the EC electrolyte, while a closed Kel-F cell with a volume of 0.5 ml was employed for the DMC electrolyte due to the solvent's high vapor pressure. In both cells, the working electrode was placed below an opening in the cell body, which was sealed with an O-ring against electrolyte leakage (inner diameter 5 mm, cross section 1 mm, ring material: FKM 75 for the EC-based, Teflon for the DMC-based electrolyte). Li foil (Alfa Aesar, ≥ 99.99%) was used as counter and reference electrode. All potentials are referenced versus Li/Li⁺. After assembly, the cell was dried in Ar for 16 hrs at 100 °C and then transferred into an Ar-filled glove box (H₂O < 1 ppm/O₂ < 0.5 ppm). Cyclic voltammograms were

recorded in a potential window of 1.5–0.02 V at scan rates of 0.1, 1 and 10 mV s⁻¹, using a Solartron Analytical Modulab potentiostat (Pstat 1MS/s). To obtain current densities, the currents recorded were normalized by the geometric surface area of the electrode, as defined by the inner diameter of the O-ring (SA_{geo} = 0.196 cm²). After cycling (five cycles at 0.1/10 mV s⁻¹, start/stop at the upper potential limit), selected electrodes were prepared for characterization by X-ray photoelectron spectroscopy (XPS). First, the electrodes were rinsed with DMC in order to remove excess salt and excess EC electrolyte by electrolyte exchange in the cell. This was repeated four times. Next, the electrode was immersed in DMC for 45–60 minutes. This procedure of solvent exchange and soaking was repeated five times. Finally, the electrode was dried in the glove box in Argon atmosphere. To protect against air, the dry electrode was transferred to the spectrometer in a hermetically sealed transport box.

XPS measurements were conducted using monochromatized Al K_α (1486.6 eV) radiation at a detection angle of 45 ° (PHI 5800 Multi Technique ESCA System, Physical Electronics). Survey and detail spectra were recorded with the analyzer set to pass energies of 93.9 eV or 29.25 eV, respectively. After probing the elemental composition of the SEI surface, depth profiles were generated by recording spectra after 2, 4, 6 and 18 minutes of successive Ar⁺ sputtering (I_{sp} ~ 1 µA; U_{sp} = 5 kV). The total sputtering time thus amounted to 2, 6, 12 and 30 minutes, with an expected sputter rate of approximately 1 nm min⁻¹, as specified by the manufacturer. Charging effects were compensated by electron irradiation of the sample via a flood gun (I_{neutr} = 3 µA). The binding energy (BE) was calibrated versus the F 1s signal of LiF at 685.0 eV,^[60] similar to our previous study.^[33] For quantitative evaluation, a Shirley-type background was subtracted from the spectra and peak fitting was performed using a weighted least-square fitting of peak components with 70% Gaussian and 30% Lorentzian character. For quantification, the peak intensities were normalized with the atomic sensitivity factors (ASF) given by the instrument manufacturer.^[60] Further details of the evaluation and peak fitting procedure are given in the discussion part and in a previous report.^[33]

Acknowledgements

We gratefully acknowledge financial support by the German Federal Ministry of Education and Research (BMBF) in the project 03X4636 C ("Li-EcoSafe – Entwicklung kostengünstiger und sicherer Lithium-Ionen-Batterien"). We also would like to thank AMG Kropfmühl (Hauzenberg, Germany) for providing the natural graphite raw material that was used for the synthesis of the SNG material, Dr. M. Rapp (ZSW Ulm, Germany), who prepared the binder-containing SNG electrodes, and Dr. M. Eckardt (Institute of Surface Chemistry and Catalysis, Ulm University) for the TEM measurements. This work contributes to the research performed at CELEST (Center for Electrochemical Energy Storage Ulm-Karlsruhe). Open access funding enabled and organized by Projekt DEAL.

Conflict of Interest

The authors declare no conflict of interest.

Keywords: electrochemistry · photoelectron spectroscopy · graphite · lithium-ion batteries · solid electrolyte interphase

- [1] J. M. Tarascon, M. Armand, *Nature* **2001**, *414*, 359–367.
- [2] B. Scrosati, J. Garche, *J. Power Sources* **2010**, *195*, 2419–2430.
- [3] A. Barrie, B. Deguilhem, S. Grolleau, M. Gerard, F. Suard, D. Riu, *J. Power Sources* **2013**, *241*, 680–689.
- [4] M. A. Hannan, M. S. H. Lipu, A. Hussain, A. Mohamed, *Renewable Sustainable Energy Rev.* **2017**, *78*, 834–854.
- [5] M. Winter, J. O. Besenhard, M. E. Spahr, P. Novák, *Adv. Mater.* **1998**, *10*, 725–763.
- [6] B. Scrosati, *Electrochim. Acta* **2000**, *45*, 2461–2466.
- [7] P. G. Bruce, B. Scrosati, J.-M. Tarascon, *Angew. Chem. Int. Ed.* **2008**, *47*, 2930–2946.
- [8] R. C. Massé, C. Liu, Y. Li, L. Mai, G. Cao, *Nat. Sci. Rev.* **2017**, *4*, 26–53.
- [9] D. Aurbach, Y. Talyosef, B. Markovsky, E. Markevich, E. Zinigrad, L. Asraf, J. S. Gnanaraj, H. J. Kim, *Electrochim. Acta* **2004**, *50*, 247–254.
- [10] K. Xu, *Chem. Rev.* **2004**, *104*, 4303–4418.
- [11] J. Kalhoff, G. G. Eshetu, D. Bresser, S. Passerini, *ChemSusChem* **2015**, *8*, 2154–2175.
- [12] S. S. Zhang, *J. Power Sources* **2006**, *162*, 1379–1394.
- [13] E. Peled, *J. Electrochem. Soc.* **1979**, *126*, 2047–2051.
- [14] C. Shen, S. Wang, Y. Jin, W. Q. Han, *ACS Appl. Mater. Interfaces* **2015**, *7*, 25441–25447.
- [15] S. K. Jeong, M. Inaba, Y. Iriyama, T. Abe, Z. Ogumi, *Electrochim. Acta* **2002**, *47*, 1975–1982.
- [16] K. Kanamura, H. Tamura, Z. i. Takehara, *J. Electroanal. Chem.* **1992**, *333*, 127–142.
- [17] R. Dédryvère, S. Leroy, H. Martinez, F. Blanchard, D. Lemordant, D. Gonbeau, *J. Phys. Chem. B* **2006**, *110*, 12986–12992.
- [18] S. K. Jeong, M. Inaba, R. Mogi, Y. Iriyama, T. Abe, Z. Ogumi, *Langmuir* **2001**, *17*, 8281–8286.
- [19] J. Zhang, X. Yao, R. K. Misra, Q. Cai, Y. Zhao, *J. Mater. Sci. Technol.* **2020**, *44*, 237–257.
- [20] D. Aurbach, B. Markovsky, A. Shechter, Y. Ein-Eli, H. Cohen, *J. Electrochem. Soc.* **1996**, *143*, 3809–3820.
- [21] D. Aurbach, A. Zaban, Y. Ein-Eli, I. Weissman, O. Chusid, B. Markovsky, M. Levi, E. Levi, A. Schechter, E. Granot, *J. Power Sources* **1997**, *68*, 91–98.
- [22] E. Peled, D. Golodnitsky, A. Ulus, V. Yufit, *Electrochim. Acta* **2004**, *50*, 391–395.
- [23] M. Nie, D. Chalasani, D. P. Abraham, Y. Chen, A. Bose, B. L. Lucht, *J. Phys. Chem. C* **2013**, *117*, 1257–1267.
- [24] P. Lanz, P. Novák, *J. Electrochem. Soc.* **2014**, *161*, A1555–A1563.
- [25] T. Kranz, S. Kranz, V. Miß, J. Schepp, B. Roling, *J. Electrochem. Soc.* **2017**, *164*, A3777–A3784.
- [26] L. S. Roselin, R. S. Juang, C. T. Hsieh, S. Sagadevan, A. Umar, R. Selvin, H. H. Hegazy, *Materials* **2019**, *12*, 1229.
- [27] P. Verma, P. Maire, P. Novák, *Electrochim. Acta* **2010**, *55*, 6332–6341.
- [28] K. Xu, A. von Cresce, *J. Mater. Chem.* **2011**, *21*, 9849–9864.
- [29] M. Gauthier, T. J. Carney, A. Grimaud, L. Giordano, N. Pour, H. H. Chang, D. P. Fenning, S. F. Lux, O. Paschos, C. Bauer, M. Filippo, S. Lupart, P. Lamp, Y. Shao-Horn, *J. Phys. Chem. Lett.* **2015**, *6*, 4653–4672.
- [30] S. J. An, J. Li, C. Daniel, D. Mohanty, S. Nagpure, D. L. Wood III, *Carbon* **2016**, *105*, 52–76.
- [31] E. Peled, S. Menkin, *J. Electrochem. Soc.* **2017**, *164*, A1703–A1719.
- [32] M. Bozorgchenani, F. Buchner, K. Forster-Tonigold, J. Kim, A. Groß, R. J. Behm, *Langmuir* **2018**, *34*, 8451–8463.
- [33] I. Weber, J. Schnaidt, B. Wang, T. Diemant, R. J. Behm, *ChemElectroChem* **2019**, *6*, 4985–4997.
- [34] M. Rapp, M. Mundsinger, S. Farsi, U. Golla-Schindler, U. Kaiser, M. Wachtler, Herstellung und Bewertung mechanisch gerundeter Graphite als Anodenmaterial für Lithium-Ionen-Batterien. Meitingen Frühjahrstagung 2016 des Arbeitskreises Kohlenstoff. 26-4-2016.
- [35] M. Mundsinger, S. Farsi, M. Rapp, U. Golla-Schindler, U. Kaiser, M. Wachtler, *Carbon* **2017**, *111*, 764–773.
- [36] M. Inaba, Z. Siroma, A. Funabiki, Z. Ogumi, T. Abe, Y. Mizutani, M. Asano, *Langmuir* **1996**, *12*, 1535–1540.
- [37] A. C. Chu, J. Y. Josefowicz, G. C. Farrington, *J. Electrochem. Soc.* **1997**, *144*, 4161–4169.
- [38] D. Alliata, R. Kötz, P. Novák, H. Siegenthaler, *Electrochem. Commun.* **2000**, *2*, 436–440.
- [39] A. Cresce, S. M. Russell, D. R. Baker, K. J. Gaskell, K. Xu, *Nano Lett.* **2014**, *14*, 1405–1412.
- [40] D. Bar-Tow, E. Peled, L. Burstein, *J. Electrochem. Soc.* **1999**, *146*, 824–832.
- [41] E. Peled, D. BarTow, A. Merson, L. Burstein, *J. New Mater. Electrochem. Syst.* **2000**, *3*, 321–328.
- [42] B. K. Antonopoulos, F. Maglia, F. Schmidt-Stein, J. P. Schmidt, H. E. Hoster, *Batteries & Supercaps* **2018**, *1*, 110–121; *Supercaps* **2018**, *1*, 110–121.
- [43] Z. T. Gossage, J. Hui, Y. Zeng, H. Flores-Zuleta, J. Rodriguez-Lopez, *Chem. Sci.* **2019**, *10*, 10749–10754.
- [44] K. Persson, V. A. Sethuraman, L. J. Hardwick, Y. Hinuma, Y. S. Meng, A. Ven, V. Srinivasan, R. Kostecki, G. Ceder, *J. Phys. Chem. Lett.* **2010**, *1*, 1176–1180.
- [45] Z. Zhang, K. Smith, R. Jervis, P. R. Shearing, T. S. Miller, D. J. L. Brett, *ACS Appl. Mater. Interfaces* **2020**, *12*, 35132–35141.
- [46] L. Wang, X. Deng, P. X. Dai, Y. G. Guo, D. Wang, L. J. Wan, *Phys. Chem. Chem. Phys.* **2012**, *14*, 7330–7336.
- [47] S. H. Kang, D. P. Abraham, A. Xiao, B. L. Lucht, *J. Power Sources* **2008**, *175*, 526–532.
- [48] A. Xiao, L. Yang, B. L. Lucht, S. H. Kang, D. P. Abraham, *J. Electrochem. Soc.* **2009**, *156*, A318–A327.
- [49] M. Nie, D. P. Abraham, D. M. Seo, Y. Chen, A. Bose, B. L. Lucht, *J. Phys. Chem. C* **2013**, *117*, 25381–25389.
- [50] M. E. Spahr, H. Buqa, A. Würsig, D. Goers, L. Hardwick, P. Novák, F. Krumeich, J. Dentzer, C. Vix-Guterl, *J. Power Sources* **2006**, *153*, 300–311.
- [51] P. Novák, J. Ufheil, H. Buqa, F. Krumeich, M. E. Spahr, D. Goers, H. Wilhelm, J. Dentzer, R. Gadiou, C. Vix-Guterl, *J. Power Sources* **2007**, *174*, 1082–1085.
- [52] Graphite Anode Material for High-energy Lithium Ion Batteries, Hitachi Reports 2009–2010 **2010**, *74*.
- [53] V. Eshkenazi, E. Peled, L. Burstein, D. Golodnitsky, *Solid State Ionics* **2004**, *170*, 83–91.
- [54] M. Tang, S. Lu, J. Newman, *J. Electrochem. Soc.* **2012**, *159*, A1775–A1785.
- [55] B. Horstmann, F. Single, A. Latz, *Curr. Opt. Electrochem.* **2019**, *13*, 61–69.
- [56] Y. G. Ryu, S. I. Pyun, *J. Electroanal. Chem.* **1997**, *433*, 97–105.
- [57] A. M. Andersson, K. Edström, *J. Electrochem. Soc.* **2001**, *148*, A1100–A1109.
- [58] L. J. Rendeck, G. S. Chottiner, D. A. Scherson, *J. Electrochem. Soc.* **2002**, *149*, E408–E412.
- [59] R. Dédryvère, H. Martinez, S. Leroy, D. Lemordant, F. Bonhomme, P. Biensan, D. Gonbeau, *J. Power Sources* **2007**, *174*, 462–468.
- [60] J. F. Moulder, W. F. Stickle, P. E. Sobol, K. D. Bomben, *Handbook of X-ray Photoelectron Spectroscopy*, (Ed.: J. Chastain) Perkin Elmer Corp., Eden Prairie/USA 1992.
- [61] D. Ensling, M. Stjern Dahl, A. Nyten, T. Gustafsson, J. O. Thomas, *J. Mater. Chem.* **2009**, *19*, 82–88.
- [62] A. M. Andersson, A. Henningson, H. Siegbahn, U. Jansson, K. Edström, *J. Power Sources* **2003**, *119*, 522–527.
- [63] R. Dédryvère, S. Laruelle, S. Grugeon, L. Gireaud, J. M. Tarascon, D. Gonbeau, *J. Electrochem. Soc.* **2005**, *152*, A689–A696.
- [64] G. V. Zhuang, K. Xu, H. Yang, T. R. Jow, P. N. Ross, *J. Phys. Chem. B* **2005**, *109*, 17567–17573.
- [65] A. Wang, S. Kadam, H. Li, S. Shi, Y. Qi, *npj Compu. Mater.* **2018**, *4*, 15.
- [66] K. Edström, M. Herstedt, D. P. Abraham, *J. Power Sources* **2006**, *153*, 380–384.
- [67] P. Niehoff, S. Passerini, M. Winter, *Langmuir* **2013**, *29*, 5806–5816.

Manuscript received: October 15, 2020

Revised manuscript received: November 24, 2020

Accepted manuscript online: November 26, 2020